Analysis of piezocone penetration under different drainage conditions with the two-phase Material Point Method

Ceccato F., Beuth L., Simonini P. (2016). Analysis of piezocone penetration under different drainage conditions with the two-phase Material Point Method. Journal of geotechnical and Geoenvironmental engineering (in press) DOI: 10.1061/(ASCE)GT.1943-5606.0001550

ANALYSIS OF PIEZOCONE PENETRATION UNDER DIFFERENT DRAINAGE CONDITIONS WITH THE TWO-PHASE MATERIAL POINT METHOD

Francesca Ceccato[1], Lars Beuth[2], Paolo Simonini[3]

Abstract: The piezocone penetration test (CPTU) is commonly used to identify the soil profile and to estimate material properties. Depending on the soil type, ranging from clay to sand, undrained, partially drained or drained conditions may occur during cone penetration. In silt and sand-clay mixtures the CPTU penetration is characterized by partially drained conditions, which are often neglected in data interpretation. The effect of drainage on CPTU measurements has been mainly studied experimentally. Numerical analyses are rare because taking into account large soil deformations, soil-water and soil-structure interactions, as well as non-linear soil behaviour is still a challenging task. This paper presents and discusses numerical simulations of CPTU in saturated soils with the two-phase Material Point Method. Soil behaviour is described with the Modified Cam Clay model. This study investigates the effects of pore pressure dissipation during penetration, cone roughness and horizontal stress state, comparing the results with experimental data. The paper discusses the effect of neglecting partial

[1] (**Corresponding author**) Ph.D., Research fellow, DICEA – University of Padua, via Ognissanti 39, 35129 Padua, Italy.: francesca.ceccato@dicea.unipd.it.
[2] Ph.D., Senior researcher, Deltares, P.O. Box 177, 2600 MH Delft, The Netherlands, e-mail: lars.beuth@deltares.nl
[3] Ph.D., Full professor, DICEA – University of Padua, via Ognissanti 39, 35129 Padua, Italy, e-mail: paolo.simonini@unipd.it

drainage in deriving the shear strength parameters for silty soils and suggests a procedure to estimate the consolidation coefficient performing CPTU at different penetration rates.

Key words: CPT/CPTU, partial drainage, two-phase MPM, consolidation, large deformations

Introduction

The cone penetration test (CPT) and its enhanced versions, piezocone (CPTU) and seismic (SCPTU), are widely used in-situ soil testing techniques employed to identify the subsoil profile and to estimate relevant soil properties. It consists in pushing a steel cone with a measuring device attached to its tip into the ground with a constant rate of 2 cm/s (Fig. 1). The derived measurements of tip resistance, q_c, sleeve friction, f_s, and pore pressure u_2 (in the case of piezocone with pore pressure transducer behind the cone shoulder) are correlated to various soil characteristics, see e.g. Lunne et al. (1997) for an overview.

Most of the existing empirical and theoretical correlations between CPT measurements and soil properties assumes fully drained conditions, typical of sand, or fully undrained conditions, typical of clay. However, in soils such as silt and sand-clay mixture, the cone penetrates in partially drained conditions, i.e. excess pore pressures are generated which partially dissipate during penetration.

Experimental evidence shows that if the pressure dissipation is relatively fast compared to the penetration rate, the soil in the vicinity of the advancing cone consolidates during penetration. Thus, higher tip resistances are found compared to those obtained in undrained conditions (House et al. 2001, Randolph and Hope 2004, Schneider et al. 2007, Kim et al. 2008, Lehane et al. 2009, Jaeger et al. 2010, Oliveira et al. 2011).

This paper investigates the effect of drainage conditions on cone penetration through advanced numerical analyses. The aim of this study is to provide a better understanding of the cone penetration process, thus leading to more accurate interpretation of field data. To this purpose, the effect of partial drainage in soil classification by means of a normalized chart and in deriving the shear strength parameters for silt-based mixtures is discussed. Moreover, a procedure to estimate the consolidation

coefficient from CPTU at variable penetration rates is proposed and applied to the field measurements by Kim et al. (2008).

In addition to the influence of drainage conditions on the measured tip resistance and pore pressure, this paper investigates the influence of the horizontal stress and the friction at the soil-cone interface too. Numerical results are compared with results by centrifuge tests on kaolin.

Three-dimensional large soil deformations, soil-water interaction, soil-cone interaction, and non-linear soil behaviour are taken into account. To the authors' knowledge such complex numerical simulations of CPTU are a novelty. Previous numerical studies assumed drained conditions, e.g. Susila and Hryciw (2003), Huang et al. (2004), Kouretzis et al. (2014), or undrained conditions, e.g. Abu-Farsakh et al. (2003), Lu et al. (2004), Beuth and Vermeer (2013), Qiu (2014). The effect of the penetration rate has been investigated numerically by Silva et al. (2006) and Yi et al. (2013). Silva et al. (2006) studied the stress distribution after cone penetration in normally consolidated and overconsolidated clay. Soil behaviour is modelled by Modified Cam Clay model. Their method is based on the cylindrical cavity expansion theory coupled with finite element method (FEM); only radial soil deformation and water flow are considered. Yi et al. (2013) carried out parametric analyses using the updated Lagrangian finite element method with logarithmic strain. Problems of mesh distortions are encountered with this method, that need to be controlled manually by remeshing. In their study, Drucker-Prager constitutive model is applied; however, the authors recognize that it overestimates the undrained shear strength of normally consolidated soils. Only a smooth soil-cone interface is considered because of numerical difficulties when frictional contact is introduced.

In the present study, large soil deformations coupled with fluid flow are simulated with a two-phase Material Point Method (MPM). MPM has been specifically developed since the '90s for large deformation analyses (Sulsky et al. 1994). Recently, the method has been extended to multiphase porous media (Abe et al. 2013, Jassim et al. 2013, Alonso and Zabala 2011).

A simple but realistic description of the soil response in a wide range of drainage conditions is achieved using the Modified Cam Clay (MCC) model (Roscoe and Burland 1968).

The properties of the soil-cone interface influence significantly the tip resistance and they should be properly considered. The soil-cone interaction is modelled with the algorithm proposed by Bardenhagen et al. (2001), which considers Coulomb's friction law. This contact formulation was originally formulated for one-phase analyses and it has been extended for two-phase analyses in the frame of the present study.

In the following sections the numerical approach is briefly presented; an extensive description of the numerical implementation exceeds the purpose of this paper, but further details can be found in the provided references.

Numerical modelling

Overview of the Material Point Method

The classical Updated Lagrangian Finite Element method (UL-FEM) has been successfully used for decades in geomechanics. However, difficulties appear when applied to large deformation problems because of numerical inaccuracies introduced by element distortions. The need to overcome this drawback led to the development of alternative methods such as Discrete Element method (DEM) (Cundall and Strack 1979), Smoothed Particle Hydrodynamic (SPH) (Lucy 1977) and MPM (Sulsky et al 1994).

The MPM belongs to the family of particle-based methods. It has been derived from the Particle-In-Cell method (PIC) used for fluid mechanics (Harlow 1955). Schreyer, Sulsky and co-workers, extended it for problems of solid mechanics (Sulsky et al., 1994, 1995). It was first applied to granular materials by Więckowski (1999, 2004) and Coetzee et al. (2005). This method has been used successfully in the study of a number of geomechanical large deformation problems such as anchor pull-out (Coetzee et al. 2005), landslides (Andresen and Andersen 2010a, Soga et al. 2015), cone penetration (Beuth and Vermeer 2013), pile installation (Phuong et al. 2014).

Multiphase MPM formulations have recently been developed (e.g. Zhang et al. 2008, Jassim et al. 2013, Abe et al. 2013). They allow to take into account the soil-water interaction, which is essential in may

geotechnical problems. These formulations has been applied to the study of dam and riverbank failure (Alonso and Zabala 2011, Bandara and Soga 2015).

In MPM, arbitrary large deformations of a body are simulated by a set of material points (MPs) which move through a computational finite element mesh. The MPs carry all the information of the continuum such as density, velocity, acceleration, stress, strain, material parameters as well as external loads. It can be regarded as an extension of the UL-FEM because the underlying finite element grid is used, as with the UL-FEM, to solve the system of equilibrium equations. However, the MP positions are updated from nodal incremental displacements at the end of each time step. The mesh is usually reset into its original state; it does not follow the deformations of the body as in UL-FEM, which prevents problems of element distortion.

To illustrate the solution procedure, let us consider a one-phase dynamic problem governed by the discretized momentum equations:

$$\boldsymbol{M\dot{v}} = \boldsymbol{F^{ext}} - \boldsymbol{F^{int}} \tag{1}$$

where $\boldsymbol{M}$ is the mass matrix, $\boldsymbol{v}$ is the nodal velocity vector, $\boldsymbol{F^{ext}}$ is the external load and $\boldsymbol{F^{int}}$ is the internal load vectors.

At the beginning of each time increment the terms of Equation 1 are initialized by mapping information from the MPs to the computational nodes of the mesh by means of the interpolation functions (Fig. 2a).

The governing equations of motion are solved for the nodal accelerations $\dot{\boldsymbol{v}}$ (Fig. 2b). These nodal values are used to update acceleration, velocity and position of MPs, as well as to compute strains and stresses at the MPs (Fig. 2c).

At the end of the time step, the mesh is usually reset into its original state or changed arbitrarily. The assignment of MPs to finite elements is updated after mesh adjustment (Fig. 2d). A detailed description of the solution procedure can be found in Sulsky et al. (1995).

The finite element grid used with the MPM must cover not only the solid in its initial configuration, but the entire region of space into which the solid is expected to move. However, only those elements which

contain MPs (active elements) contribute to the equation of motion. Spatial integration is only performed over the volume inside the finite element mesh that is covered by material. The larger mesh therefore does not lead to a significant additional computational effort.

The software applied in this study is an enhanced version of the original MPM, which has been extensively validated for quasi-static and dynamic problems in geomechanics by Al-Kafaji (2013). It has been used in a number of geotechnical applications, see e.g. Phuong et al. (2016), Soga et al. (2015), Alonso et al. (2015), Yerro et al. (2014), Jassim et al. (2013).

In this version of MPM, volumetric locking, often generated by the use of low order elements, is mitigated by a strain smoothening technique (Detournay and Dzik, 2006).

The movement of MPs across element boundaries is known to cause noise in the solution (see e.g. Steffen et al. 2008, Andersen and Andersen 2010b). With the used enhanced MPM variant, Gauss integration is applied in fully filled element (element in which the sum of the volumes of the contained MPs is greater than 90% of the element volume) (Beuth et al. 2011). This approach proved to reduce significantly the noise (Al-Kafaji 2013, Jassim et al. 2013) and it gives reasonably good results with a lower computational cost compared to other implementations such as GIMP (Bardenhagen and Kobe 2004) and CPDI (Sadeghirad et al. 2011).

The two-phase Material Point Method

In order to take into account soil-water interaction the mathematical model must consider the equilibrium of the water and the soil skeleton as separate phases. Several two-phase formulations have been published; Zienkiewicz et al. (1980) provide a detailed overview of the various formulations. The formulation adopted in this study has the solid velocity v and fluid velocity w as primary unknown variables. Only a brief description of the derivation is provided in the following; the reader is referred to Jassim et al. (2013) and Al-Kafaji (2013) for further details.

The momentum equation of the water phase is:

$$\rho_w \dot{\boldsymbol{w}} + \frac{n\gamma_w}{k}(\boldsymbol{v} - \boldsymbol{w}) = \nabla p_w + \rho_w \boldsymbol{g} \tag{2}$$

where ρ_w and γ_w are the density and the unit weight of the water, k is the Darcy's permeability, n is the porosity, p_w is the pore water pressure and $\boldsymbol{g}$ is the gravity vector. The second term on the left hand side represents the interaction between solid and fluid.

The momentum equation for the mixture is:

$$(1-n)\rho_s \dot{\boldsymbol{v}} + n\rho_w \dot{\boldsymbol{w}} = \nabla \cdot (\boldsymbol{\sigma}' + \boldsymbol{I}p_w) + \rho_{sat}\boldsymbol{g} \tag{3}$$

where ρ_s is the density of the solid grains, $\rho_{sat} = n\ \rho_w + (1-n)\ \rho_s$ is the saturated density, $\boldsymbol{\sigma}'$ is the effective stress, and $\boldsymbol{I}$=[1,1,1,0,0,0].

The excess pore pressure increment can be calculated from the mass balance equation for the water phase:

$$\dot{p}_w = \frac{K_w}{n}[(1-n)\boldsymbol{\nabla} \cdot \boldsymbol{v} + n\boldsymbol{\nabla} \cdot \boldsymbol{w}] \tag{4}$$

where K_w is the bulk modulus of the water. The effective stress rate is calculated from the strain rate by means of the soil constitutive model. This study adopts the co-rotational rate of Kirchhoff stress following van Langen (1991).

The weak form of the momentum balance equations is derived by multiplying (2) and (3) by a test function and then integrating over the current configuration. The terms involving the stress are integrated by parts and the divergence theorem is applied. The acceleration, velocity, and displacement fields are approximated by means of finite element shape functions ($\boldsymbol{N}$). With the available MPM code, 4-noded tetrahedral elements with piecewise linear shape functions are used.

The discretized momentum equations can be written as:

$$\boldsymbol{M_w}\dot{\boldsymbol{w}} = \boldsymbol{F_w^{ext}} - \boldsymbol{F_w^{int}} - \boldsymbol{F_w^{drag}} \tag{5}$$

$$\boldsymbol{M_s}\dot{\boldsymbol{v}} + \bar{\boldsymbol{M}}_{\boldsymbol{w}}\dot{\boldsymbol{w}} = \boldsymbol{F^{ext}} - \boldsymbol{F^{int}} \tag{6}$$

where the subscripts *s* and *w* indicate the soil and water phase respectively; no subscript indicates that the quantity belongs to the mixture. $\boldsymbol{F_w^{drag}} = \int_V n\gamma_w k^{-1}\boldsymbol{N^T N}dV(\boldsymbol{v}-\boldsymbol{w})$ denotes a drag force computed from the relative water velocity ($\boldsymbol{w}$ – $\boldsymbol{v}$), which takes into account the solid-fluid interaction. The mass matrices for the fluid and the soil skeleton are defined as: $\boldsymbol{M_w} = \int_V \rho_w \boldsymbol{N^T N}dV$ and $\boldsymbol{M_s} = \int_V (1-n)\rho_s \boldsymbol{N^T N}dV$. Matrix $\bar{\boldsymbol{M}}_{\boldsymbol{w}}$ is formed using the density $n\rho_w$ in place of ρ_w. For numerical implementation, the lumped mass matrices are used (Jassim et al. 2013).

In the present study, the explicit Euler-Cromer time integration scheme is used (Cromer 1981). This means that the acceleration is calculated explicitly and the velocity is updated from it implicitly. This solution algorithm is conditionally stable, i.e. the time step size (Δt) has to be smaller than a critical time increment (Δt_{crit}). Jassim et al. (2013) observed that the Courant-Friedrichs-Lewy (CFL) condition ($\Delta t_{crit,CFL} = l_{min}/c_p$, l_{min} = minimum length of the element, c_p = velocity of the undrained compression wave) ensures the stability of the analyses considered in their paper. Miermet et al. (2015) showed that the CFL is not a sufficient condition and improved the definition of the critical time step by adding a permeability-dependent term:

$$\Delta t_{crit} = \min\left(\Delta t_{crit,CFL}; [2k(n\rho_{sat} + (1-2n)\rho_w)]/n\gamma_w\right) \tag{7}$$

The MPM solution procedure follows Jassim et al. (2013). The acceleration of the fluid is calculated by solving Equation (5). It is subsequently used to obtain the acceleration of the solid from Equation (6). The velocities and the momentum of MPs are updated from the nodal accelerations of each phase. The nodal velocities are then calculated from the nodal momentum and used to compute the strain rate at MP location. The mass balance equation (Eq. 4) and the soil constitutive law give the change of excess pore pressure and effective stress respectively. The displacement and position of each MP are updated according to the velocity of the solid phase.

In drained and undrained conditions the presence of water can be taken into account in a simplified way.

In the first case, the pressure dissipates nearly instantaneously, therefore the presence of water can be neglected. In the latter case, the velocity of the water and the velocity of the soil skeleton coincide, i.e. $\boldsymbol{v} = \boldsymbol{w}$. The soil behaves as a one-phase material and the momentum equation for the soil-water mixture (Eq. 6) reduces to Equation 1 in which the saturated mass matrix is used. This approach is computationally more efficient as only the momentum equation of the mixture is solved.

In undrained conditions, the stress state can be described in terms of total stresses or effective stresses. In the second case, the excess pore pressures can be computed by means of the so-called Effective Stress Analysis, which is based on the assumption of strain compatibility between the soil skeleton and the enclosed pore water (Vermeer 1993).

The pore pressure rate is calculated using the volumetric strain $\dot{\varepsilon}_{vol}$:

$$\dot{p}_w = \frac{K_w}{n} \dot{\varepsilon}_{vol} \tag{8}$$

The effective stress increment is calculated with the soil constitutive model.

The constitutive model

The soil response is modelled with the Modified Cam Clay model (MCC) (Roscoe and Burland 1968); which has been introduced in MPM following the implementation by Nøst (2011). It takes into account most of the important features of soil behavior such as non-linear soil response, hardening behavior, occurrence of shear and volumetric deformations during yielding and stress-path dependency of the shear strength.

Viscous effects and anisotropy are known to influence the tip resistance in clay (Beuth and Vermeer 2013, Chung et al. 2006, Randolph 2004). However, this is not taken into account in this study. The aim is to investigate the influence of drainage conditions of the soil surrounding the cone and the MCC model has been widely used to describe clay response in both drained and undrained conditions (Silva et al. 2006, Mahmoodzadeh et al. 2015).

In this study, the initial stress state is always assumed to lie on the yield surface. The material parameters

assumed for the numerical analyses are summarized in Table 1. They are typical of kaolin (Silva et al. 2006), which is one of the most used soil in laboratory tests on artificially reconstructed samples, thus allowing the comparison between numerical results and experimental data.

Geometry and discretization

The cone penetration is essentially an axisymmetric problem. However, in this study a 20° slice is considered instead of a simpler 2D geometry because the available code is fully 3D. The cone is slightly rounded in order to circumvent numerical problems induced by a discontinuous edge at the base of the cone. Apart from this modification, the dimensions of the penetrometer correspond to those of a standard penetrometer: the apex angle is 60º and the cone diameter (D) is 0.036m.

The size and the refinement of the mesh have been determined through preliminary analyses as a compromise between computational cost and accuracy. It extends 14D below the tip, at the beginning of the computation, and 8D in radial direction. It counts 13221 tetrahedral elements. 105634 MPs are located in the initially active elements. In order to further reduce problems of grid-crossing errors, and prevent small elements to become empty, 20 MPs are initially located inside each element near and directly below the cone, while 10 or 4 MPs are placed inside elements further away from the cone. A higher density of MPs in the region where more severe deformations are expected improves the quality of the analysis. Figure 3 shows the geometry and discretization of the CPT problem.

The penetrometer moves downward by a prescribed velocity of 2 cm/s applied at the nodes of the structure, which therefore behaves as a rigid body. Displacements are constrained in normal direction at the lateral mesh surfaces, while the bottom of the mesh is fully fixed. The radial boundaries of the 20^o slice are impermeable since they correspond to symmetry axes of the problem, while the bottom and the outside boundaries are permeable.

In order to keep the fine mesh always around the cone, the so-called moving mesh procedure is adopted (Beuth 2012, Phuong et al. 2016). This procedure exploits the fact that in MPM all the properties of the continuum are stored at the MPs, thus the mesh can be freely redefined at the end of each time step because it does not store any permanent information. It consists in adjusting the mesh to the movement

of the cone after each time step, ensuring that the penetrometer surface coincides with element boundaries throughout the simulation.

The mesh region adjacent to the penetrometer moves with the same displacement as the cone (Fig. 3b). The elements of this zone keep the same shape during the computation, while the elements in the compressed zone below the cone reduce their vertical length. The discretization has been determined in such a way that the elements of the compressed zone keep a reasonable aspect ratio throughout the analysis.

The soil-structure interaction is modelled with an MPM-specific algorithm proposed by Bardenhagen et al. (2001) which is presented in Appendix. The algorithm automatically detects the contact nodes, but an additional benefit of the moving mesh approach is that the need of identifying the new soil-structure interface during the computation is eliminated because the interface nodes coincide with the geometry of the cone throughout the computation. As a consequence, the unit normal vectors, which are required in the contact algorithm, do not change and hence the inaccuracy related to recomputing them is eliminated (Al-Kafaji 2013).

An external vertical stress $\sigma'_{v0} = 50$ kPa is applied on the top surface of the soil, thus simulating an initial position of the cone at about 5m depth. Indeed, assuming a submerged unit weight of 10 kN/m^3, the 5m-soil column can be reproduced by such a vertical stress. A further penetration of the cone for 10D is simulated.

Since the gradient of the vertical stress is negligible compared to the stress level developed during the penetration, the material weight is neglected, i.e. the initial stresses are constant with depth and the pore pressure is zero. Computed pore pressures are excess pore pressures. The initial vertical and horizontal effective stress are $\sigma'_{v0} = 50$ kPa and $\sigma'_{h0} = 34$ kPa respectively. This corresponds to an anisotropic state with $K = \sigma'_{h0}/\sigma'_{v0} = 0.68$ which is a typical value of the coefficient of earth pressure at rest for Kaolin (Stewart 1992).

The effect of the drainage condition is investigated by changing the Darcy permeability k, while keeping the standard penetration rate $v = 0.02$ m/s. The variation of k as a consequence of soil compression is

neglected, thus k is isotropic and constant throughout the computation.

Results

Effect of drainage conditions

Finnie and Randolph (1994) showed that the effect of soil drainage can be taken into account by introducing a normalized penetration rate, also called normalized velocity, which is defined as

$$V = \frac{vD}{c_v} \tag{9}$$

where v is the penetration rate, D the cone diameter and c_v the soil vertical consolidation coefficient. Indeed, the consolidation process near the advancing cone is not only affected by the permeability, but also the compressibility of the soil, the probe diameter and penetration rate play a significant role.

Assuming that the soil compressibility during penetration is well described by the virgin compression index λ, the consolidation coefficient can be estimated with Equation 10, as suggested by Schneider et al. (2007)

$$c_v = \frac{k(1+e_0)\sigma'_{v0}}{\lambda\gamma_w} \tag{10}$$

Errore. L'origine riferimento non è stata trovata. shows the tip stress over the normalized cone displacement in case of smooth contact for undrained, partially drained (with V = 1.2 and V = 12.0) and drained conditions. Here, small numerical noise has been filtered out by means of a running average smoothing with a bandwidth of 0.03 normalized cone displacement. The steady state tip stress, which corresponds to the tip resistance q_c, is reached after a penetration depth which ranges from 5D, in drained conditions, to 7D, in undrained conditions.

In undrained conditions, the net tip resistance (q_c-σ_{v0}, σ_{v0} = in-situ total vertical stress) is proportional to the undrained shear strength (s_u) through a cone factor ($N_c = q_c$-σ_{v0}/s_u), which is a function of the cone roughness, the in-situ stress state and the rigidity index $I_r = G/s_u$ (G = shear modulus) (Yu and

Mitchell 1998). The cone factor obtained in this study for a smooth cone in undrained conditions is 9.6. This value is in agreement with other numerical studies when considering similar conditions (rigidity index, cone roughness, anisotropic stress state). For example, Lu et al. (2004), using Arbitrary Lagrangian-Eulerian method and Tresca material model, suggested a cone factor relationship which gives a value of 9.55 for the parameters of this study. For similar rigidity index, but in isotropic conditions, Beuth (2012) obtained a value of 10.2 applying a quasi-static implementation of MPM; and Qui et al. (2014) obtained a value of 10.7 using Coupled Eulerian-Lagrangian method.

The tip resistance increases with the decrease of the normalized penetration rate *V:* from 163 kPa in fully undrained conditions to 215 kPa in fully drained conditions. In case of $V = 1.2$ the tip resistance is only 4% lower than the drained value, and in case of $V = 12$ the tip resistance is only 4% higher than the undrained value. This agrees with the observed excess pore pressure distribution (Fig. 5). Approximately undrained behavior is observed for $V = 12$ at which the excess pore pressure next to the tip is about 120 kPa. At a distance of about 1.2D in radial direction and 0.5D below the tip, the excess pore pressure is nearly equal to one-half of the pore pressure near the cone. For $V = 1.2$ the behavior is nearly drained and the excess pore pressure is about 30 kPa. The gradient of excess pore pressure is lower than in the previous case. Indeed, one-half of the excess pore pressure near the tip is found only at a distance of about 2.5D in radial direction and 1.5D below the tip. The gradients of the excess pore pressure distribution after CPTU penetration govern the dissipation response when performing dissipation tests to estimate the consolidation coefficient. For this reason, theoretical solutions based on undrained penetration should be applied with care when interpreting dissipation tests possibly performed after a partially drained penetration (Ceccato and Simonini 2016).

The average effective stress path of an element next to the cone surface is plotted in Figure 6 for different normalized penetration rates. The position of this element is fixed with respect to the cone face, which moves downward while MPs pass through it changing its average stress state. The initial condition is identical for the considered cases: the mean effective stress is $p'_0 = 40$ kPa and the deviatoric stress is $q_0 = 15.5$ kPa. It is assumed that this stress state lies on the yield surface. The initial preconsolidation pressure p_{c0} is 47 kPa.

As the cone penetrates, the soil yields and the stress path moves toward the critical state line (CSL) in the p'-q plane. The undrained path is typical for normally consolidated clays. The stress path for a normalized penetration rate $V = 12$ initially overlaps the undrained stress path, but the final values of p' and q are higher because of consolidation effects. The mean effective stress p' and deviatoric stress q at steady state increase reducing the normalized rate V, i.e. moving from undrained to drained conditions, as result of the pore pressure dissipation during cone penetration.

Assuming the undrained penetration as a reference condition, the normalized resistance and the normalized pore pressure can be respectively defined with Equations 11 and 12

$$\frac{q_{c,net}}{q_{c,ref}} = \frac{q_c - \sigma_{v0}}{q_{c,undrained} - \sigma_{v0}} \tag{11}$$

$$\frac{\Delta u}{\Delta u_{ref}} = \frac{\Delta u}{\Delta u_{undrained}} \tag{12}$$

where $q_{c,undrained}$ and $\Delta u_{undrained}$ are respectively the tip resistance and the excess pore pressure in undrained conditions.

The relative importance of the excess pore pressure on the net cone resistance can be quantified with the pore pressure parameter B_q defined as (Senneset et al. 1982):

$$B_q = \frac{\Delta u}{q_c - \sigma_{v0}} \tag{13}$$

This parameter is often used in engineering practice to identify the soil type or estimate geotechnical properties.

Figure 7 shows the variation of the normalized cone resistance ($q_{c,net}/q_{c,ref}$), the normalized pore pressure ($\Delta u/\Delta u_{ref}$) and the pore pressure parameter (B_q) with the normalized penetration rate. Constant values of these normalized parameters are obtained for $V < 0.2$ (drained conditions) and $V > 60$ (undrained conditions). This agrees with experimental studies in which the transition to fully drained conditions is observed for V between 0.01 and 4 while the transition to fully undrained conditions is observed in the range 10-100; see e.g. Randolph and Hope (2004), Schneider et al. (2007), Oliveira et al. (2011),

Mahmoodzadeh and Randolph (2014). Differences can be attributed to the effects of soil characteristics as well as the method used to estimate the consolidation coefficient by different authors.

Influence of the horizontal stress state

Since the tip stress is highly influenced by the horizontal effective stress, it is interesting to investigate the effect of an initial stress anisotropy. To this aim, two additional cases have been numerically investigated, namely an isotropic stress state with $K = \sigma'_{h0}/\sigma'_{v0} = 50/50 = 1$ and an anisotropic stress state with the horizontal effective stress higher than the vertical one, namely $K = \sigma'_{h0}/\sigma'_{v0} = 62.5/50 = 1.25$. For the sake of simplicity, the initial mean effective and deviatoric stress p'_0 and q_0 are assumed to lie on the initial yield surface, whose size increases according to the higher initial horizontal stress. These initial stress states should not be considered representative of typical conditions in the field, where the initial stress state is a function of the overconsolidation ratio (OCR). Indeed, natural soils usually consolidate one-dimensionally and only after unloading (leading to OCR > 1) they will show K higher than the normally compressed coefficient of earth pressure at rest. Different paths may be generated by complex three-dimensional loading conditions, e.g. on slopes, near construction works or excavations, and obtained in the laboratory where samples can be prepared with a desired stress state.

Figure 8 shows that the stress state influences the tip resistance q_c; the lowest resistances are observed for $K = 0.68$ ($\sigma'_{h0} = 34$ kPa) and the highest for $K = 1.25$ ($\sigma'_{h0} = 62.5$ kPa). However, the normalized resistance and the normalized pore pressure are not significantly influenced by the initial horizontal stress, as shown in Figure 9. This conclusion does not hold if the initial stress state does not lie on the yield surface, i.e. overconsolidated states are considered. It has been shown that the normalized resistance decreases with OCR (Schneider et al. 2007, Silva et al. 2006).

It is interesting to note that the soil element close to the middle of the cone surface is subjected to an effective stress path that is significantly affected by the initial horizontal effective stress for the whole range of drainage conditions (Fig. 10). In addition, increasing the initial size of the ellipse, as a consequence of induced stress anisotropy, leads to higher soil resistances with all the considered stress paths moving toward the CSL.

Influence of friction coefficient of the soil-cone interface

The cone roughness is simulated assigning a friction coefficient μ of the soil-cone interface which varies between zero, i.e. smooth contact, and 0.42, i.e. very rough contact.

In drained conditions, the tip resistance increases linearly with the friction coefficient, while in partially drained and undrained conditions the increase is non-linear (Fig. 11). This non-linear trend is probably an effect of the non-linear constitutive model and the frictional contact algorithm (the maximum contact force is a function of the normal stress, see the Appendix). It can be explained observing that both effective stress and pore pressure contribute to the tip resistance, but the friction with the cone mainly increases the effective stress, being the cone-water contact assumed smooth. Other numerical studies, which performed total stress analyses with Tresca material model and adhesive contact (the maximum contact force is a constant), found a linear increase of q_c with cone roughness, see e.g. Lu et al. (2004) and Beuth and Vermeer (2013). Further investigations are required to explain this result.

Figure 12 shows the normalized tip resistance as a function of the normalized velocity V for different values of the friction coefficient. The maximum normalized resistance increases with the cone roughness from a value of 1.4 for μ = 0 to a value of 2.4 for μ= 0.42.

Data can be interpolated by a backbone curve described by the equation

$$\frac{q_{c,net}}{q_{c,ref}} = 1 + \frac{1 - q_{c,drained}/q_{c,ref}}{1 + (V/V_{50})^c} \tag{14}$$

where $q_{c,drained}$ is the net tip resistance in drained conditions, V_{50} is the normalized velocity corresponding to the penetration velocity at which the net cone resistance is an average between the drained and undrained value and the coefficient c is the maximum rate of change in $q_{c,net}/q_{c,ref}$ with V (DeJong and Randolph 2012).

The coefficients corresponding to the best fit of the numerical data are summarized in Table 2. $q_{c,drained}/q_{c,ref}$ increases with μ because the resistance ratio is proportional to the friction coefficient. V_{50} varies between 3.36 and 7.26, with an average of 5.72. c varies between 0.82 and 1.51, with an average

of 1.07. The spread of published data on kaolin can be reasonably captured for variations of V_{50} from about 0.3 to 8 and c from about 0.5 to 1.5 (De Jong and Randolph 2012).

The effect of friction coefficient on the normalized pore pressure is negligible (Fig. 13). Higher values of μ generate lower pore pressure factors (Fig. 14). This means that the relative importance of the pore pressure on the tip resistance decreases by increasing the cone roughness. This is explained by observing that the friction with the cone generates higher shear stresses in the soil, but it does not change significantly the pore pressure, which is mainly a function of the volumetric strain. The tip stress increases mainly because the effective stress increases, and this is more evident for low values of V.

The general trend of normalized pore pressure versus normalized velocity can be effectively captured by

$$\frac{\Delta u}{\Delta u_{ref}} = 1 - \frac{1}{1 + (V/V'_{50})^{c'}} \tag{15}$$

where V'_{50} is the normalized velocity corresponding to the penetration velocity at which one-half of the excess pore pressure for undrained penetration is mobilized; and the coefficient c' is the maximum rate of change in $\Delta u/\Delta u_{ref}$ with V (DeJong and Randolph 2012). DeJong and Randolph (2012) implicitly assumed $V_{50}=V'_{50}$ and $c=c'$; however, more generally, different values can be considered.

The coefficients corresponding to the best fit of the numerical data are c'=1 and V'_{50}=2.8; these are in good agreement with the results by DeJong and Randolph (2012), who found c'=1 and V'_{50}=3 by fitting a larger number of data from experimental and numerical studies on clay.

Reasonable values of μ for low plasticity clay in contact with steel lie between 0.2 and 0.35 (Lemos and Vaughan 2000). Potyondy (1961) suggested an interface friction angle equal to one-half the critical soil's friction angle, which corresponds to a friction coefficient of 0.21 in this case.

For μ between 0.2 and 0.3, the numerical results fit reasonably well the experimental results on kaolin by Randolph and Hope (2004) and Schneider et al. (2007) (Fig. 12). Differences can be attributed to the fact that the real tested material may be characterized by slightly different material parameters form

the one assumed in the numerical model and to the method adopted to estimate the consolidation coefficient, used to calculate the normalized velocity, in the experiments.

Estimation of coefficient of consolidation by CPTU at different rate

The consolidation coefficient can be estimated by performing CPTU at different penetration rates. For example, House et al. (2001) suggested to estimate c_v by the so-called twitch test. This method consists in decreasing (or increasing) the penetration rate in steps in which the cone is pushed for 1 or 2 diameters. The idea is to determine the consolidation coefficient that adjust the normalized tip resistance or the normalized pore pressure to reference backbone curves. Several expressions of these curves have been suggested in the literature (see e.g. Randolph 2004, Oliveira et al. 2008), but the authors consider equations (14) and (15) the most appropriate for practical applications.

It is important to mention that the coefficients $q_{c,drained}/q_{c,ref}$, V_{50} and c of equation (14) vary in a relatively wide range, as a function of soil properties, thus it is very difficult to suggest a reference curve for general use. In particular, the value of $q_{c,drained}/q_{c,ref}$ ranges approximately between 2 and 3.7 for centrifuge tests on normally consolidated kaolin (Schneider et al. 2007, Randolph and Hope 2001, Oliveira et al. 2008), but it may reach values of 10 in silts (Finnie and Randolph, 1994). Moreover, it is often difficult to determine in field tests because of the impractically slow penetration rate required for fully drained penetration in soils with relatively low permeability such as clay and silty-clay.

In contrast, the coefficients V'_{50} and c' of equation (15) vary in a relatively narrow range, therefore it is easier to define a reference curve for normally consolidated soils; c'=1 and V'_{50}=2.8 can be reasonably assumed.

Note that c, c' and $q_{c,drained}/q_{c,ref}$ are independent of the consolidation coefficient used to normalize the result, on the contrary V'_{50} and V_{50} depend on v, D and c_v. This means that equations (14) and (15) can be alternatively written in terms of absolute penetration velocity v without adjusting c, c' and $q_{c,drained}/q_{c,ref}$.

The values of the rate at which the excess pore pressure is half the one generated in undrained conditions

(v'_{50}) or at which the net tip resistance is the average between drained and undrained conditions (v_{50}) can be determined by curve fitting of the in situ data. The penetration rate and the normalized penetration rate are related through equation (9), from which the consolidation coefficient can be estimated once a reference V has been determined.

Note that the reference value V'_{50}=2.8 has been determined with the consolidation coefficient of equation (10), where the virgin compression index λ is used to characterize the soil's compressibility. In this study isotropic permeability is assumed (k_v=k_h), therefore $c_v \approx c_h$, but in the field, the permeability can be significantly higher in horizontal direction than in vertical direction. Since the water flow mainly occurs in horizontal direction, the CPTU provides an estimation of c_h rather than c_v.

The data collected by Kim et al. (2008) in two test sites are considered to illustrate the procedure to estimate the consolidation coefficient from field test at variable penetration rate. Site 1 (SR18) was located in Carroll County, Indiana, USA. Site 2 (SR49) is located in Jasper County, Indiana. In both sites the tests performed on silty clay are considered.

The normalized excess pore pressure over the penetration velocity is plotted in Figure 15. The values of the penetration rate at which the normalized pore pressure is 0.50 (v'_{50}) are obtained by curve fitting imposing c'=1. Then, the consolidation coefficient is determined by means of Equation 9 assuming V=2.8.

Table 3 compares the coefficients estimated with the proposed procedure with the coefficients obtained with conventional laboratory tests as reported by Kim et al (2008). There is good agreement with the measured and the estimated values, thus validating the procedure.

Considerations on interpretation of CPTU measurements is silty soils

Several factors render the interpretation of CPTU data in silty deposits very difficult. For example, they are often highly heterogeneous, their mechanical behavior differs from pure sand or pure clay, and penetration can occur in partially drained conditions. Indeed, silty deposits are characterized by a consolidation coefficient that can vary in very wide range: from 10^{-3} to 10^{-4} m^2/s for silty sand to 10^{-6}

to 10^{-7} m^2/s for silty clay. For standard CPTU the normalized rate varies approximately between 1 and more than 500, which corresponds to the range of partially drained conditions.

Figure 16 shows the classification chart proposed by Schneider et al. (2008), which allows soil classification based on the net tip resistance and the excess pore pressure. Increasing the normalized penetration rate, the points move toward the bottom-right corner as result of the lower tip resistances and higher water pressures obtained because of partial consolidation. For this reason, in order to avoid misinterpretation of the soil type, the penetration rate should be carefully controlled.

The net resistance and pore pressure corresponding to undrained conditions lie in the zone of clay with low rigidity index. For partially drained conditions, the points fall into the zone of transitional soils. Typical correlations based on drained or undrained penetration are unreliable if applied to transitional soils (Schneider et al. 2008) as demonstrated in the following.

If the silt is (wrongly) assumed to behave like an (undrained) clay-like material, because of partially drained conditions, the undrained shear strength s_u would be overestimated as effect of the higher measured tip resistance. The ratio between the estimated and the true shear strength ($s_{u,ref}$) is proportional to the normalized resistance:

$$\frac{s_u}{s_{u,ref}} = \frac{q_{c,net}}{q_{c,ref}} \tag{16}$$

Considering the numerical results of this study for μ=0.2, the maximum value of $s_u/s_{u,ref}$ is 2. However, experimental studies on different materials showed that the maximum normalized resistance may reach values of 10 in silts (Finnie and Randolph, 1994), with an average of 3 (Oliveira et al. 2011, De Jong and Randolph 2012). This means that neglecting the partially drained conditions leads to a significant overestimation of the undrained shear strength.

If the silt is (wrongly) assumed to behave like a (drained) sand-like material, the application of empirical formulas will lead to an underestimation of the friction angle. The error highly depends on the approach which is applied. Empirical correlations based on q_c, such as those proposed for example by Robertson

and Campanella (1983), Kulhawy and Mayne (1990) and Houlsby and Hitchmann (1988) amongst other, are widely used in practice. For the soil parameters of this study, assuming an underestimation of the tip resistance of about 50%, the friction angle estimated with the aforementioned correlations may be underestimated of more than 3°. However, higher errors are likely when considering a different type of soil.

Concluding remarks

In this paper, a recently implemented two-phase Material Point Method featuring a contact algorithm is presented and used to simulate piezocone tests in a wide range of drainage conditions. Numerical results agree well with experimental data obtained from laboratory piezocone penetration tests in artificially reconstructed kaolin. This method takes into account large deformation of soil, dissipation of pore pressure during penetration, cone roughness as well as non-linear soil behavior, which is modeled with the MCC material model.

The cone resistance increases with the decrease of the normalized penetration rate, while the pore pressure decreases. Indeed, the soil in the vicinity of the advancing cone consolidates, developing larger shear strength and stiffness, as confirmed by the stress path experienced by a soil element next to the cone. Partially drained conditions are found for normalized rates between 0.2 and 60, which are typical of transitional soils.

The cone roughness plays a significant influence on the numerical results and, therefore, it cannot be neglected in the numerical analyses. The tip resistance and the resistance ratio increases with the cone roughness while the normalized pore pressure does not change significantly.

Reference curves for the trend of normalized tip resistance and normalized pore pressure as function of the normalized penetration rate are proposed. These curves may be used to estimate the consolidation coefficient by performing piezocone tests at different rates. Considering the range of all published data it should be noted that the parameters c' and V'_{50} of the normalized pore pressure curve varies in a narrower range compared to the normalized resistance fitting parameters. It is suggested to consider the reference normalized pore pressure curve to estimate the consolidation coefficient by variable rate

CPTU. The method proposed in this study has been validated with the data published by Kim et al. (2008).

This study emphasizes that, in transitional soils, considering the effect of penetration rate on the measured tip resistance and pore pressure is essential. During field testing the penetration rate should be carefully controlled because deviation from the standard rate of 2cm/s or temporary interruption of the test may lead to incorrect soil classification when using reference charts.

Special attention should be paid in estimating material parameters because common approaches based on the assumptions of drained or undrained conditions are no longer valid in transitional soils. Neglecting the effect of partial drainage can lead to significant overestimation of the undrained shear strength of clayey silts or underestimation of the friction angle of silty sands. If partially drained conditions are suspected for the considered deposit, results should be interpreted with care and cross correlated with laboratory data. Alternatively, one can perform CPTU at different penetration rates to determine the undrained and drained resistance.

Acknowledgments

The authors thank prof. Pieter Vermeer for his strong support without which this work would have been much more difficult and Dr-Ing. Issam Al-Kafaji, former Deltares researcher, for his contributions to the research efforts leading to this publication.

Appendix: Modelling of soil-structure interaction

MPM is able to model non-slip contact between bodies without any special contact formulation. At the contact the bodies' velocities are identical because they belong to the same vector field. No interpenetration or sliding is allowed. However, frictional sliding generally occurs at the contact surface. This requires a specific algorithm to be simulated. In this study, the contact algorithm proposed by Bardenhagen et al. (2001) is adopted and briefly illustrated in the following.

Let us consider two bodies A and B in contact at time t. The single body velocities $\boldsymbol{v}_{k,A}$, $\boldsymbol{v}_{k,B}$ and the velocity of the combined system $\boldsymbol{v}_{k,S}$ are computed at each node by solving the respective equations of

motion. A certain node *k* is identified as a contact node when the velocity of the single body differs form the velocity of the combined system. If the bodies are approaching and the tangential contact force is greater than the maximum tangential force allowed by the contact law, the single body velocity must be corrected as follows:

$$\tilde{\boldsymbol{v}}_{\boldsymbol{k,A}} = \boldsymbol{v}_{\boldsymbol{k,A}} + \boldsymbol{c}_{\boldsymbol{k,norm}} + \boldsymbol{c}_{\boldsymbol{k,tan}} \tag{17}$$

where $\boldsymbol{c}_{\boldsymbol{k,norm}}$ is the correction for the normal component, preventing interpenetration, and $\boldsymbol{c}_{\boldsymbol{k,tan}}$ is the correction for the tangential component.

This correction is equivalent to applying the following contact forces:

$$\boldsymbol{f}_{\boldsymbol{k,norm}} = \frac{m_{k,A}}{\Delta t}\boldsymbol{c}_{\boldsymbol{k,norm}} \tag{18}$$

$$\boldsymbol{f}_{\boldsymbol{k,tan}} = \frac{m_{k,A}}{\Delta t}\boldsymbol{c}_{\boldsymbol{k,tan}} \tag{19}$$

where $m_{k,A}$ is the nodal mass and Δt the time step size.

The correction of the normal component is calculated in such a way that the normal components of the new single body velocity and of the combined bodies $\boldsymbol{v}_{\mathbf{k,s}}$ are equal, i.e.:

$$\boldsymbol{c}_{\boldsymbol{k,norm}} = -\left[\left(\boldsymbol{v}_{\boldsymbol{k,A}} - \boldsymbol{v}_{\boldsymbol{k,S}}\right) \cdot \boldsymbol{n}_{\boldsymbol{k,A}}\right]\boldsymbol{n}_{\boldsymbol{k,A}} \tag{20}$$

where $\boldsymbol{n}_{\boldsymbol{k,A}}$ is the unit outward normal vector of body *A* at node *k*.

The maximum contact force depends on the friction coefficient μ:

$$\boldsymbol{f}_{\boldsymbol{k,\tan max}} = \left(\mu\left|\boldsymbol{f}_{k,norm}\right|\right)\boldsymbol{t}_{\boldsymbol{k}} \tag{21}$$

where $\boldsymbol{t}_{\boldsymbol{k}}$ is the tangential unit vector.

Combining Equations 17 to 21, the corrected velocity takes the following expression:

$$\tilde{\boldsymbol{v}}_{k,A} = \boldsymbol{v}_{k,A} - [(\boldsymbol{v}_{k,A} - \boldsymbol{v}_{k,S}) \cdot \boldsymbol{n}_{k,A}]\boldsymbol{n}_{k,A} + [(\boldsymbol{v}_{k,A} - \boldsymbol{v}_{k,S}) \cdot \boldsymbol{n}_{k,A}]\mu \boldsymbol{t}_k \quad (22)$$

The aforementioned contact algorithm has been extended for the two-phase analyses in order to take into account the interaction between the water phase and the impermeable structure. Immediately after having solved the momentum equation for the fluid (Eq. 5), the water velocities and accelerations must be corrected.

In order to prevent the inflow of water, the normal component of the fluid velocity w_{norm} must be equal to the normal component of the structure velocity $v_{cone,norm}$. The corrected velocity for the water at the contact node *k* takes the form:

$$\tilde{\boldsymbol{w}} = \boldsymbol{w} - [(\boldsymbol{w} - \boldsymbol{v}_{cone}) \cdot \boldsymbol{n}_k]\boldsymbol{n}_k \quad (23)$$

where $\boldsymbol{n}_k$ is the outward normal unit vector to soil body at node *k*. The corrected nodal acceleration is recalculated from the corrected nodal velocity and used in the momentum equation for the mixture (Eq. 6), which is solved to obtain the acceleration of the solid phase. At this step, the velocity of the solid is predicted and then corrected according to the algorithm presented by Bardenhagen et al. (2001).

The scheme of the two-phase MPM computation with the introduction of the contact algorithm is illustrated in Figure 17. It is important to note that the correction for the nodal water velocity is applied between the solution of the momentum equation for the water and the solution of the momentum equation for the mixture. The correction for the solid velocity is applied just before the updating of MP information.

References

Abe, K., Kenichi S., and Bandara S. (2013) "Material point method for coupled hydromechanical problems." *Journal of Geotechnical and Geoenvironmental Engineering*, 140(3)

Abu-Farsakh, M., Tumay, M., and Voyiadjis, G. (2003). "Numerical parametric study of piezocone penetration test in clays." *International Journal of Geomechanics*, *3*(2), 170-181.

Al-Kafaji, I. K. J. (2013). *Formulation of a Dynamic Material Point Method (MPM) for Geomechanical Problems*. Ph. D. thesis, University of Stuttgart, Germany.

Alonso, E. E., Yerro, A., and Pinyol, N. M. (2015). "Recent developments of the Material Point Method for the simulation of landslides." *IOP Conference Series: Earth and Environmental Science*, 26(SEPTEMBER), 012003.

Alonso, E. and F. Zabala (2011). "Progressive failure of Aznalcollar dam using the material point method." *Geotechnique 61*(9), 795–808.

Andersen, S. and L. Andersen (2010a). "Modelling of landslides with the material-point method." *Computational Geosciences*, 14 (1), 137-147.

Andersen, S., and L. Andersen (2010b). "Analysis of spatial interpolation in the material-point method." *Computers and structures*, *88*(7), 506-518.

Bandara, S., and K. Soga. (2015). "Coupling of soil deformation and pore fluid flow using material point method." *Computers and Geotechnics*, 63, 199-214.

Bardenhagen, S. G., and Kober, E. M. (2004). "The generalized interpolation material point method." *Computer Modeling in Engineering and Sciences*, *5*(6), 477-496.

Bardenhagen, S., J. E. Guilkey, K. Roessig, J. Brackbill, W. Witzel, and J. Foster (2001). "Improved contact algorithm for the material point method and application to stress propagation in granular material." *Computer Modeling in Engineering and Sciences, 2(4)*, 509–522.

Beuth, L. (2012). *Formulation and Application of a Quasi-Static Material Point Method*. Ph. D. thesis, University of Stuttgart.

Beuth, L. and P. A. Vermeer (2013). "Large deformation analysis of cone penetration testing in undrained clay." *In: Installation Effects in Geotechnical Engineering*, Hicks et al. (eds), Taylor & Francis Group, London, 2013

Beuth, L., Więckowski, Z., and Vermeer, P. A. (2011). "Solution of quasi-static large-strain problems by the material point method." *International Journal for Numerical and Analytical Methods in Geomechanics*, *35*(13), 1451-1465.

Ceccato, F., & Simonini, P. (2016). "Numerical study of partially drained penetration and pore pressure dissipation in piezocone test." *Acta Geotechnica*, 1-15, DOI: 10.1007/s11440-016-0448-6.

Chung, S. F., Randolph, M. F., and Schneider, J. A. (2006). "Effect of penetration rate on penetrometer resistance in clay." *Journal of geotechnical and geoenvironmental engineering*, *132*(9), 1188-1196.

Coetzee, C. J., P. A. Vermeer, and A. H. Basson (2005, August). "The modelling of anchors using the material point method." *International Journal for Numerical and Analytical Methods in Geomechanics* 29 (9), 879-895.

Cromer, A.(1981) "Stable solutions using the Euler approximation." *American Journal of Physics*, 49(5), 455-459, DOI: 10.1119/1.12478.

Cundall, P. A. and O. D. Strack (1979). "A discrete numerical model for granular assemblies." *Geotechnique* 29 (1), 47-65.

DeJong, J. T., and Randolph, M. (2012). "Influence of partial consolidation during cone penetration on estimated soil behavior type and pore pressure dissipation measurements." *Journal of Geotechnical and Geoenvironmental Engineering*, *138*(7), 777-788.

Detournay, C. and E. Dzik (2006). "Nodal mixed discretization for tetrahedral elements." In *4th international FLAC symposium, numerical modeling in geomechanics*. Minnesota Itasca Consulting Group, Inc. Paper, Number 07-02.

Finnie, I. M. S. and M. F. Randolph (1994). "Punch-through and liquefaction induced failure of shallow foundations on calcareous sediments." In *Int. Conf. on Behavior of Offshore Structures*, Volume 187, Zielona Gora, Poland, pp. 217-230.

Harlow F.H. (1955). "A Machine Calculation Method for Hydrodynamic Problems." Los Alamos

House, A. R., Oliveira, J. R. M., and Randolph, M. F. (2001). "Evaluating the coefficient of consolidation using penetration tests." *International Journal of Physical Modelling in Geotechnics*, *1*(3), 17-26.

Houlsby, G. T., and Hitchman, R. (1988). "Calibration chamber tests of a cone penetrometer in sand." *Geotechnique*, *38*(1), 39-44.

Huang, W., Sheng, D., Sloan, S. W., and Yu, H. S. (2004). "Finite element analysis of cone penetration in cohesionless soil." *Computers and Geotechnics*, *31*(7), 517-528.

Jaeger, R., J. DeJong, R. W. Boulanger, H. E. Low, and M. Randolph (2010). "Variable penetration rate CPT in an intermediate soil." In Omnipress (Ed.), *Proc. 2nd Int. Symp. on Cone Penetration Testing*, Madison.

Jassim, I., D. Stolle, and P. Vermeer (2013). "Two-phase dynamic analysis by material point method." *International Journal for Numerical and Analytical Methods in Geomechanics* 37, 2502-2522.

Kim, K., M. Prezzi, R. Salgado, and W. Lee (2008). "Effect of penetration rate on cone penetration resistance in saturated clayey soils." *Journal of geotechnical and Geoenvironmental engineering*, 134 (8), 1142-1153.

Kouretzis, G. P., Sheng, D., and Wang, D. (2014). "Numerical simulation of cone penetration testing using a new critical state constitutive model for sand." *Computers and Geotechnics*, *56*, 50-60.

Kulhawy, F. H., and Mayne, P. W. (1990). *Manual on estimating soil properties for foundation design* (No. EPRI-EL-6800). Electric Power Research Inst., Palo Alto, CA (USA); Cornell Univ., Ithaca, NY (USA). Geotechnical Engineering Group.

Lehane, B., C. O'Loughlin, M. Randolph, and C. Gaudin (2009). "Rate effects on penetrometer resistance in kaolin." *Geotechnique* 59 (1), 41-52.

Lemos, L. and P. Vaughan (2000). "Clay-interface shear resistance." *Geotechnique* 50 (1), 55-64.

Lu, Q., Y. Hu, M. F. Randolph, and I. C. Bugarski (2004, January). "A numerical study of cone penetration in clay." *Geotechnique 54*(4), 257–267.

Lucy, L. B. (1977). "A numerical approach to the testing of the fission hypothesis." *The astronomical journal* 82, 1013-1024.

Lunne, T., P. Robertson, and J. Powell (1997). *Cone penetration testing in geotechnical practice*. EF Spon/Routledge Publ., New York.

Mahmoodzadeh, H., and Randolph, M. F. (2014). "Penetrometer Testing: Effect of Partial Consolidation on Subsequent Dissipation Response." *Journal of Geotechnical and Geoenvironmental Engineering*, 140 (6), DOI: 10.1061/(ASCE)GT.1943-5606.0001114.

Mahmoodzadeh, H., Randolph, M. F., and Wang, D. (2014). "Numerical simulation of piezocone dissipation test in clays." *Géotechnique*, *64*(8), 657-666.

Mieremet, M., D. Stolle, F. Ceccato, K. Vuik (2015). "Numerical Stability for Modelling Of Dynamic Two-Phase Interaction*." International Journal for Numerical and Analytical Methods in Geomechanics*. DOI: 10.1002/nag.2483

Nøst, Hilde Aas. (2011). *Undrained soft soil modelling with the Material Point Method*. Master, thesis, Norwegian University of science and technology.

Oliveira, J., M. Almeida, H. Motta, and M. Almeida (2011). "Influence of penetration rate on penetrometer resistance." *Journal of Geotechnical and Geoenvironmental Engineering* 137 (7), 695-703.

Potyondy, J. (1961). "Skin friction between various soils and construction materials." *Geotechnique* 11(4), 339-353.

Phuong, N. T. V., van Tol, A. F., Elkadi, A. S. K., and Rohe, A. (2016). "Numerical investigation of pile installation effects in sand using material point method." *Computers and Geotechnics*, Elsevier Ltd,

73, 58–71.

Phuong N.T.V., Tol A.F. van, Elkadi A.S.K., Rohe A. (2014). "Modelling of pile installation using the material point method (MPM)". *In: Proc. 8th European Conference on Numerical Methods in Geotechnical Engineering* (NUMGE 2014), Delft, The Netherlands. pp. 271-276. DOI:10.1201/b17017-50

Qiu, G. (2014). "Numerical analysis of penetration tests in soils." In J. Grabe (Ed.), *Ports for Container Ships of future generations*, Number 1920, Hamburg, Germany, pp. 183-196.

Randolph, M. (2004). "Characterisation of soft sediments for offshore applications." In V. da Fonseca and Mayne (Eds.), *Proc. 2nd Int. Conf. on Site Characterisation*, Porto, Rotterdam, pp. 209-232. Millpress.

Randolph, M. and S. Hope (2004). "Effect of cone velocity on cone resistance and excess pore pressures." *In Proc., Int. Symp. on Engineering Practice and Performance of Soft Deposits*, pp. 147-152. Yodagawa Kogisha Co., Ltd.

Robertson, P. K., and Campanella, R. G. (1983). "Interpretation of cone penetration tests. Part I: Sand." *Canadian geotechnical journal*, *20*(4), 718-733.

Roscoe, K.H., and Burland, J.B. (1968). "On the generalised stress–strain behaviour of wet clay." In *Engineering plasticity*. Edited by J. Heyman and F.P. Leckie. Cambridge University Press, New York, pp. 535–609.

Sadeghirad, A., Brannon, R. M., and Burghardt, J. (2011). "A convected particle domain interpolation technique to extend applicability of the material point method for problems involving massive deformations." *International Journal for Numerical Methods in Engineering*, *86*(12), 1435-1456.

Schneider, J., B. M. Lehane, and F. Schnaid (2007). "Velocity effects on piezocone measurements in normally and over consolidated clays." *International Journal of Physical Modelling in Geotechnics* *7*(2), 23–34.

Schneider, J. A., Randolph, M. F., Mayne, P. W., and Ramsey, N. R. (2008). "Analysis of factors influencing soil classification using normalized piezocone tip resistance and pore pressure parameters." *Journal of geotechnical and geoenvironmental engineering*, *134*(11), 1569-1586.

Senneset, K., Janubu, N. and Svano, G. (1982). "Strength and deformation parameters from cone penetration tests." *Proc. 2nd Eur. Symp. on Penetration Testing*, Amsterdam, Vol. 2, 863-870, Balkema, Rotterdam.

Silva, M. F., D. J. White, and M. D. Bolton (2006). "An analytical study of the effect of penetration rate on piezocone tests in clay." *International journal for numerical and analytical methods in geomechanics 30*(6), 501–527.

Soga, K., Alonso, E., Yerro, A., Kumar, K., and Bandara, S. (2015). "Trends in large-deformation analysis of landslide mass movements with particular emphasis on the material point method." *Géotechnique*, 1-26. DOI: 10.1680/jgeot.15.LM.005

Steffen, M., Kirby, R. M., and Berzins, M. (2008). "Analysis and reduction of quadrature errors in the material point method (MPM)." *International Journal for Numerical Methods in Engineering*, *76*(6), 922-948.

Stewart, D. P. (1992). *Lateral loading of piled bridge abutments due to embankment construction*. Ph.D. thesis, Univ. of Western Australia, Crawley, Australia.

Sulsky, D., Z. Chen, and H. Schreyer (1994). "A particle method for hystory-dependent materials." *Computer Methods in Applied Mechanics and Engineering 118*(1-2), 179–196.

Sulsky, D., Zhou, S. J., and Schreyer, H. L. (1995). "Application of a particle-in-cell method to solid mechanics." *Computer Physics Communications*, *87*(1), 236-252.

Susila, E., and Hryciw, R. D. (2003). "Large displacement FEM modelling of the cone penetration test (CPT) in normally consolidated sand." *International Journal for Numerical and Analytical Methods in Geomechanics*, *27*(7), 585-602.

Van Langen, H. (1991). *Numerical analysis of soil-structure interaction.* Doctoral dissertation, TU Delft, Delft University of Technology.

Vermeer, P. A. (1993). *PLAXIS 2D Reference Manual Version 5*. Balkema, Rotterdam / Brookfield.

Wieckowski, Z., S.K. Youn, and J.H. Yeon (1999). "A particle -in-cell solution to the silo discharging problem." *International Journal for Numerical Methods in Engineering,* 45 (9), 1203-1225.

Wieckowski, Z. (2004, October). "The material point method in large strain engineering problems." *Computer Methods in Applied Mechanics and Engineering 193*(39), 4417–4438.

Yi, J., M. Randolph, S. Goh, and F. Lee (2012, August). "A numerical study of cone penetration in fine-grained soils allowing for consolidation effects." *Geotechnique 62*(8), 707–719.

Yerro, A., Alonso, E. E., and Pinyol, N. M. (2014). "Run-out of landslides in brittle soils . A MPM analysis." *Geomechanics from Micro to Macro,* 1(1), 977–982

Yu, H., J. Mitchell (1998). "Analysis of cone resistance: review of methods." *Journal of Geotech Geoenvironmental Engineering* 124 (2), 140–9.

Zhang, D. Z., Q. Zou, W. B. Vander Heyden, and X. Ma (2008, March). "Material point method applied to multiphase fows." *Journal of Computational Physics* 227 (6), 3159-3173.

Zienkiewicz, O., C. Chang, and P. Bettess (1980). "Drained, undrained, consolidating and dynamic behaviour assumptions in soils." *Geotechnique* 30 (4), 385-395.

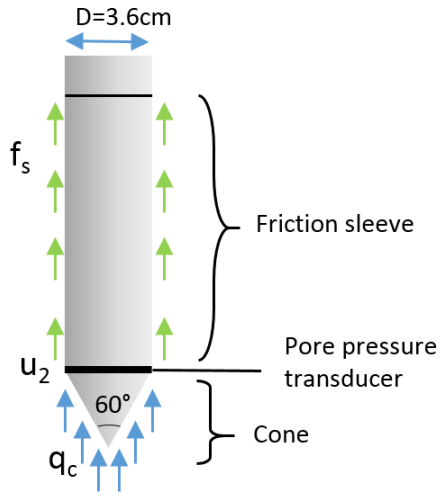

Figure 1 Simplified representation of the CPTU device

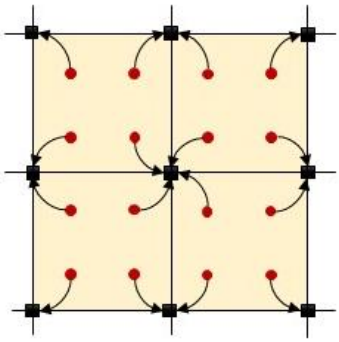

(a) Interpolate state variables to the grid nodes

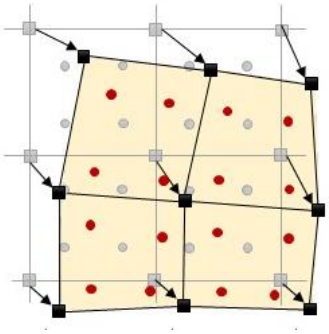

(b) Solve the governing equations of motion at the nodes

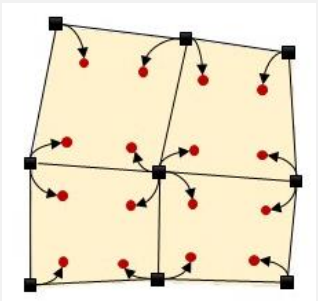

(c) Update MP velocity, stress, strains etc.

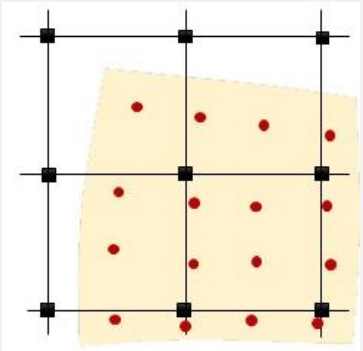

(d) Reset the mesh and update MP housekeeping

Figure 2 Computation scheme of MPM

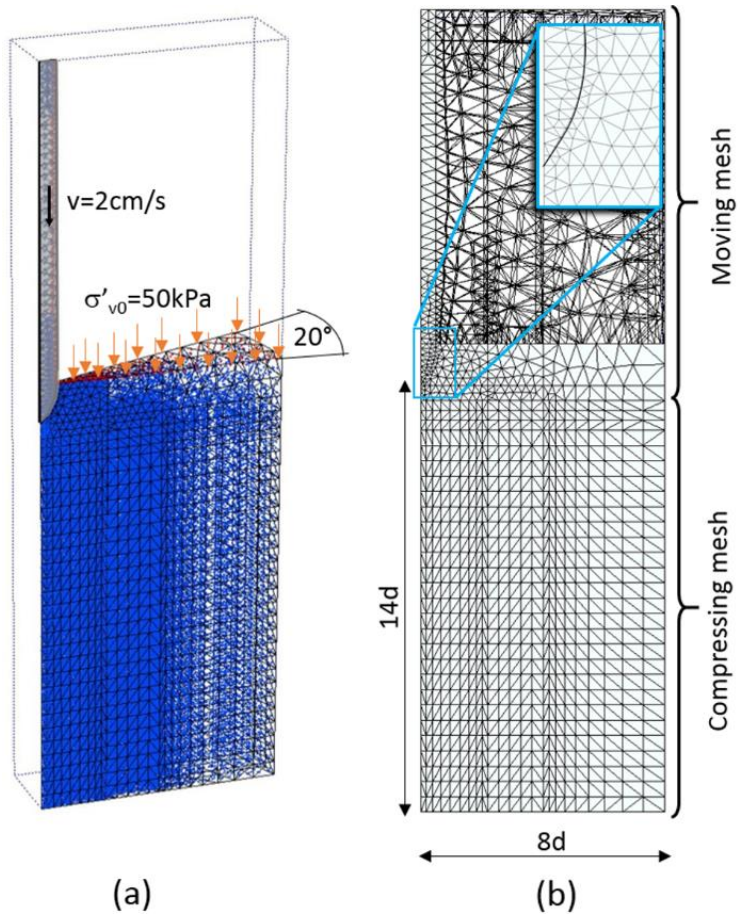

Figure 3 Geometry and discretization of the CPT problem.

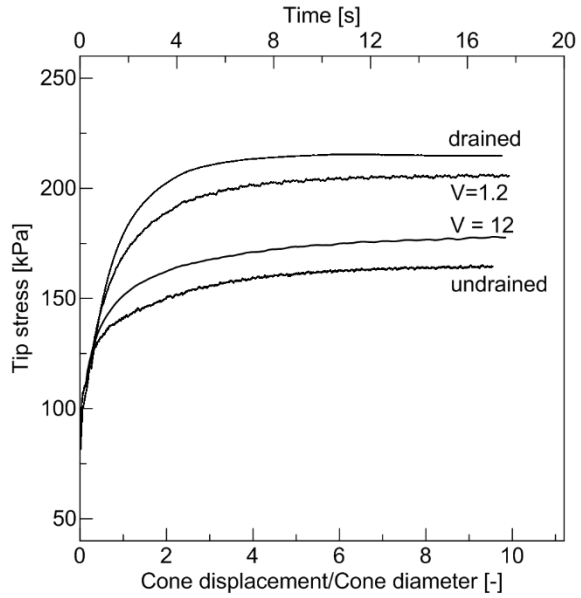

Figure 4 Tip stress over normalized penetration for different drainage conditions.

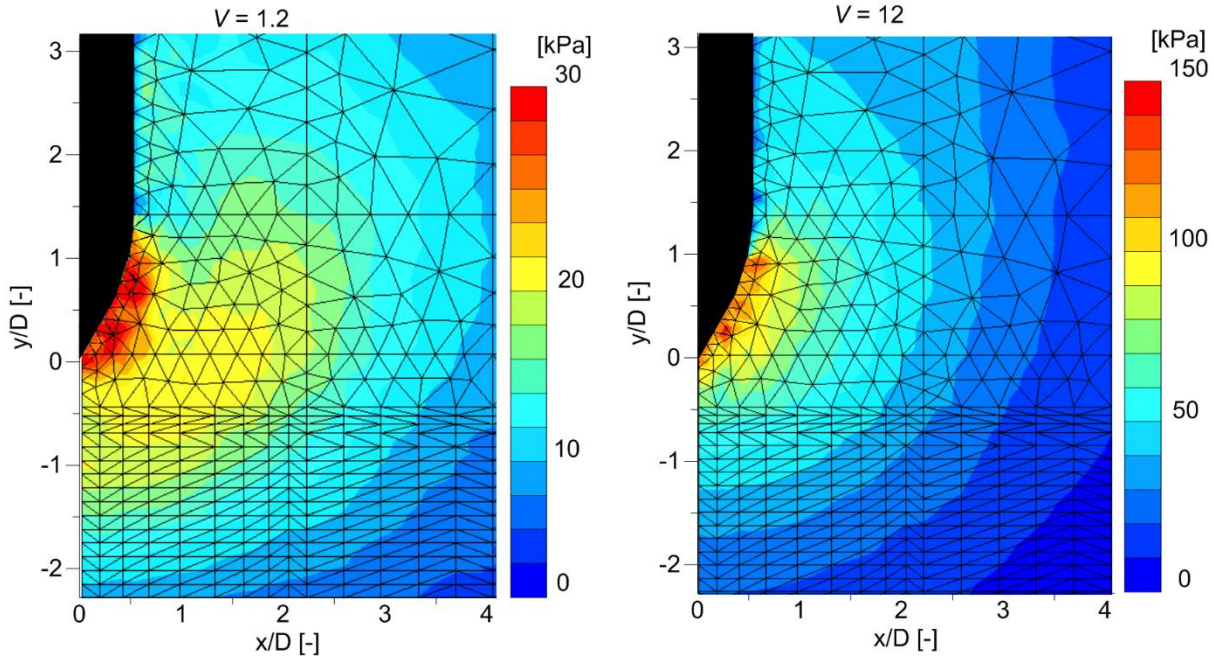

Figure 5 Excess pore pressure for the case V=1.2 (left) and V=12 (right)

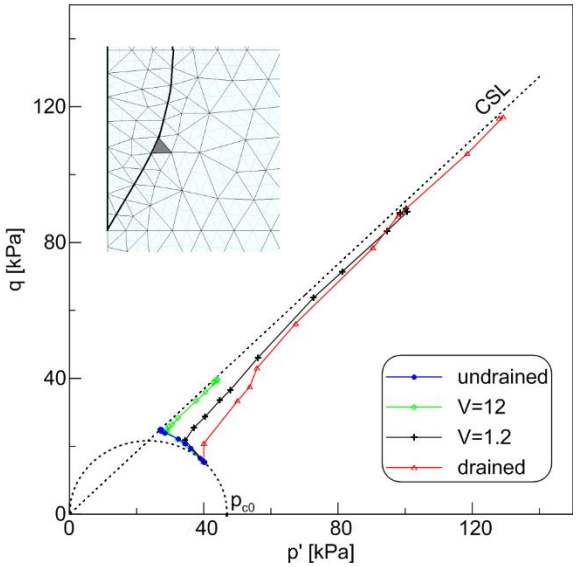

Figure 6 Effective stress path of an element next to the cone surface for several values of the normalized penetration velocity.

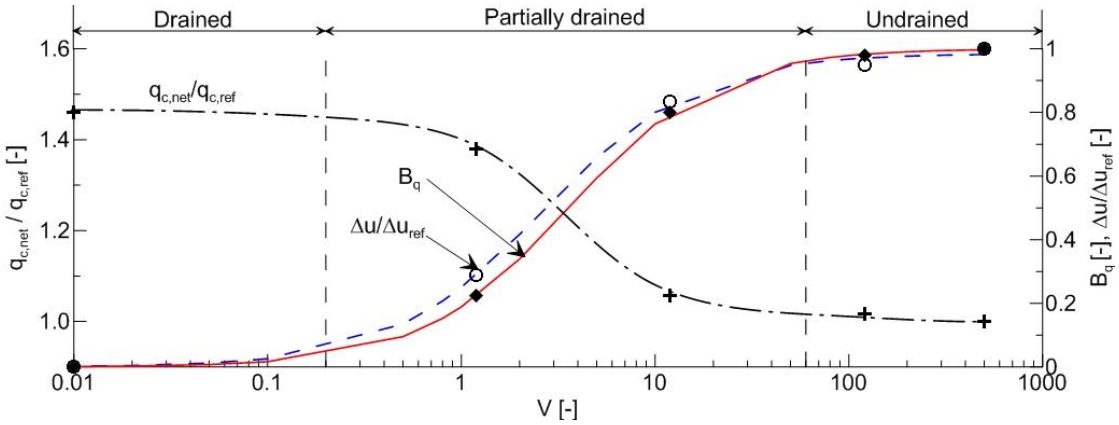

Figure 7 Normalized resistance, normalized pore pressure and pore pressure factor over normalized penetration rate.

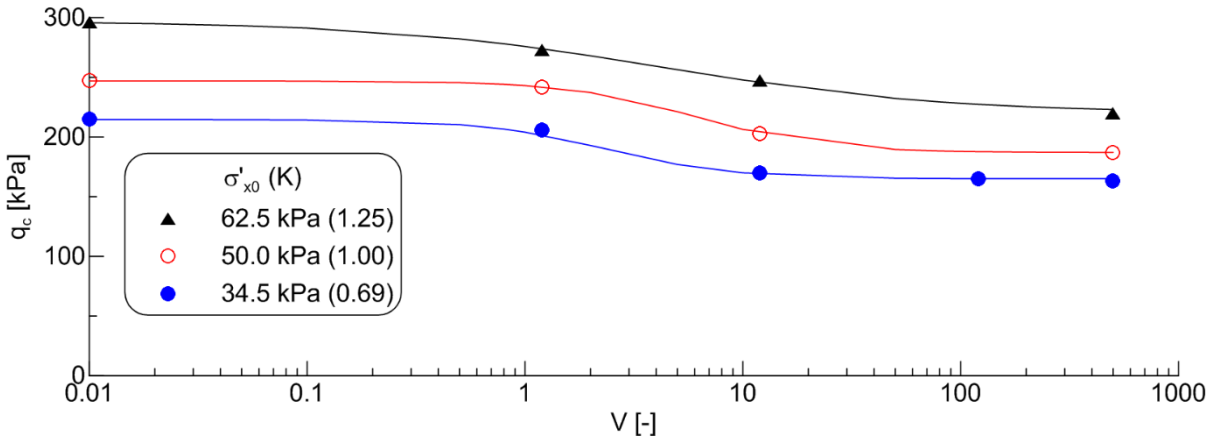

Figure 8 Tip resistance q_c over normalized penetration velocity V for several initial horizontal stress.

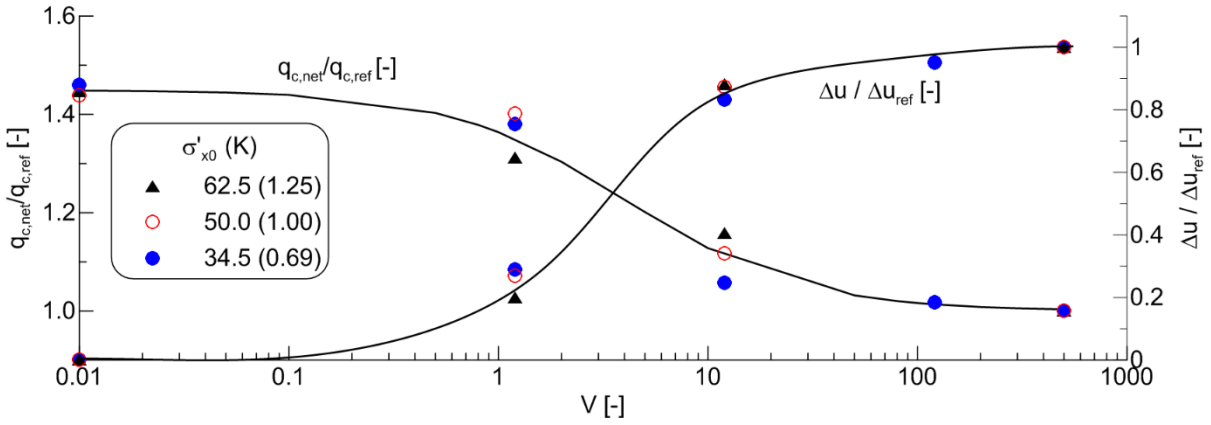

Figure 9 Normalized resistance and normalized pore pressure over normalized penetration resistance V, for different values of the initial horizontal stress.

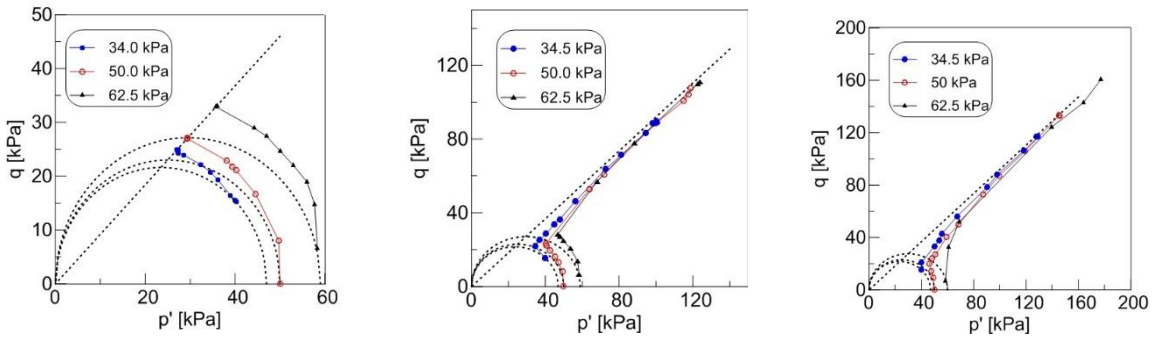

(a) (b) (c)

Figure 10 Effective stress path for different values of the initial horizontal stress in case of undrained conditions (a), partially drained conditions V=1.2 (b) and drained conditions (c)

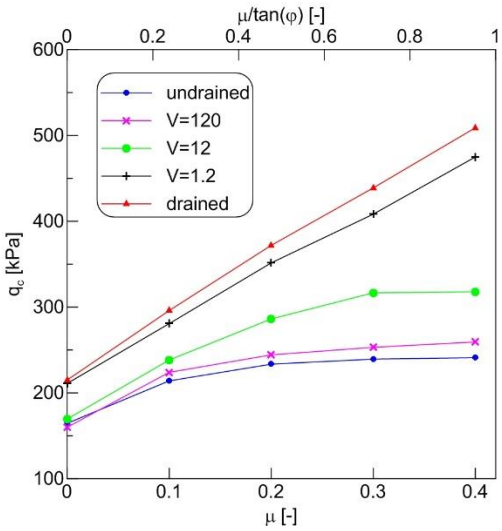

Figure 11 Tip resistance q_c as function of the friction coefficient μ, for different penetration velocities V.

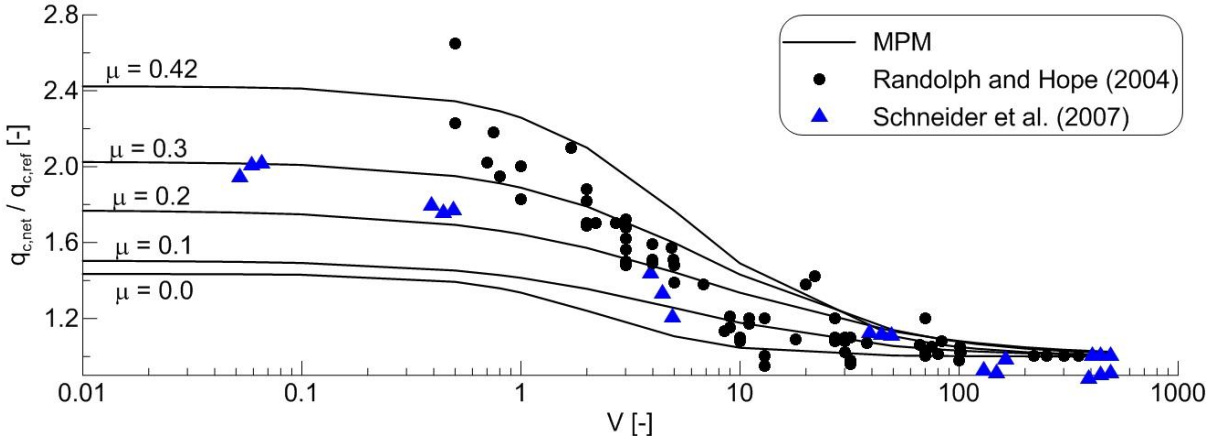

Figure 12 normalized resistance q_{net}/q_{ref} over normalized penetration resistance V, for several values of the friction coefficient. Comparison with centrifuge tests (Randolph and Hope 2004, Schneider et al 2007).

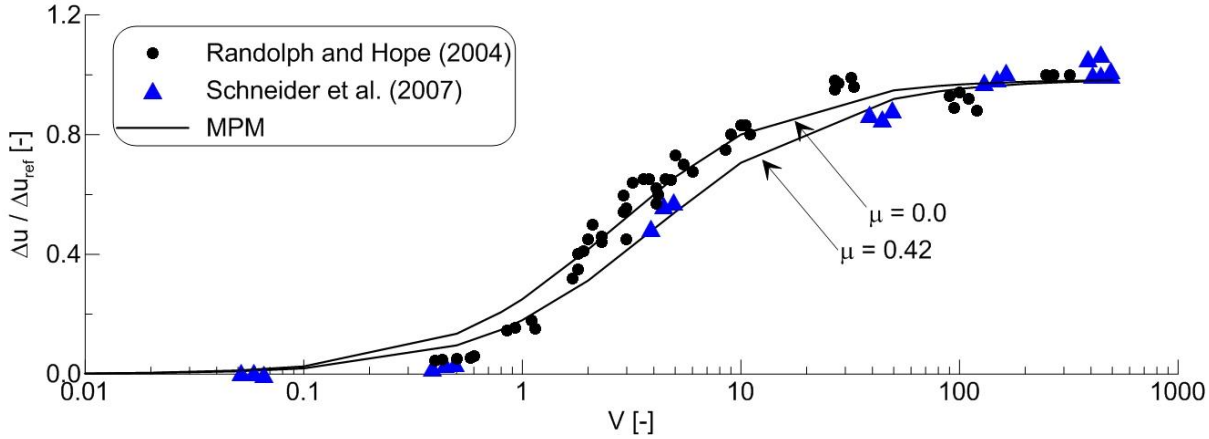

Figure 13 Normalized pore pressure $\Delta u/\Delta u_{ref}$ over normalized penetration resistance V, for several values of the friction coefficient. Comparison with centrifuge tests (Randolph and Hope 2004, Schneider et al 2007).

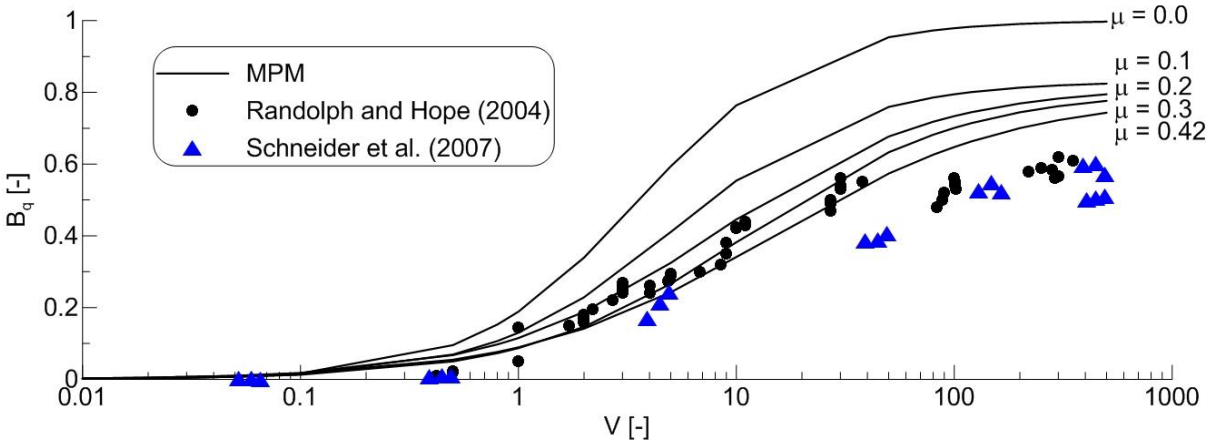

Figure 14 Pore pressure parameter B_q over normalized penetration velocity V, for several values of the friction coefficient μ. Comparison with centrifuge tests (Randolph and Hope 2004, Schneider et al 2007).

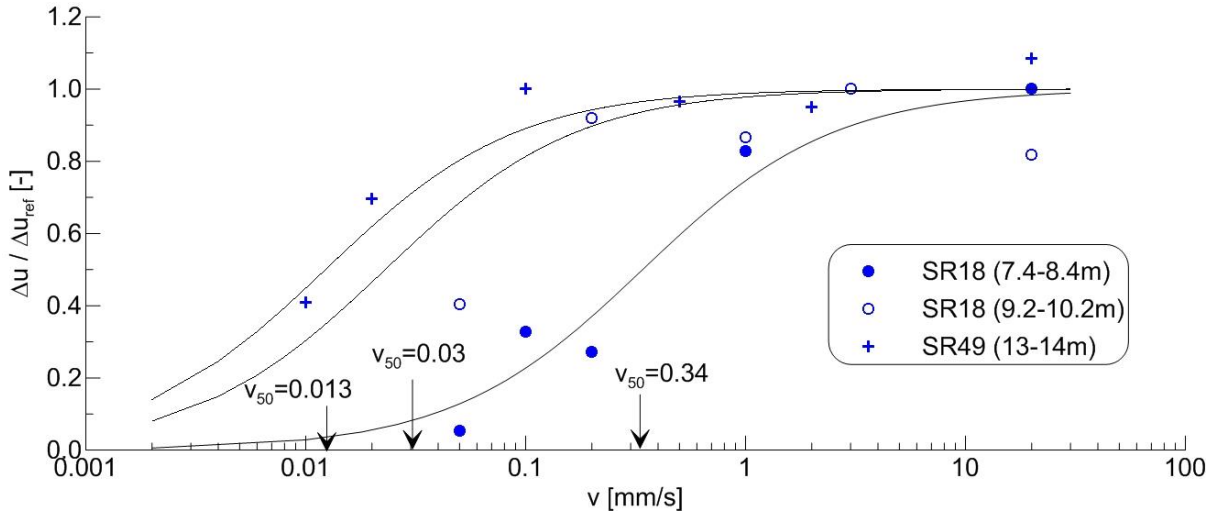

Figure 15 Normalized pore pressure over penetration velocity by Kim et al. (2008)

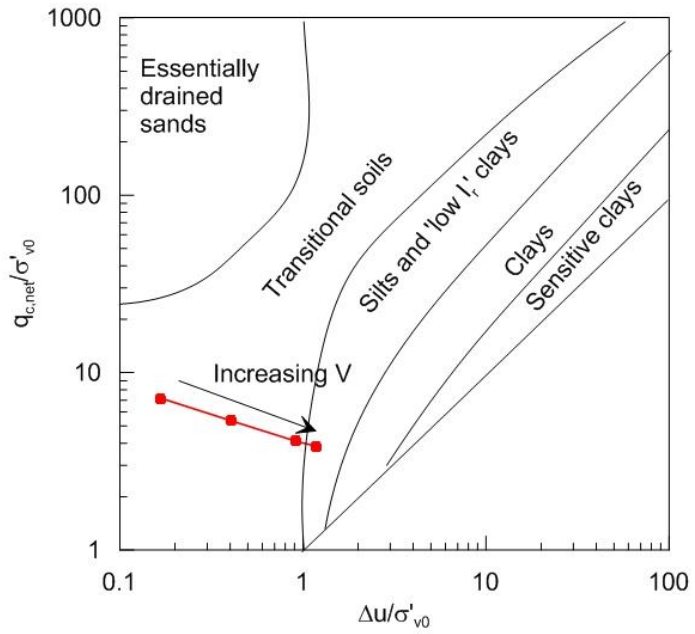

Figure 16 Effect of normalized penetration rate in the soil classification chart proposed by Schneider et al. (2008)

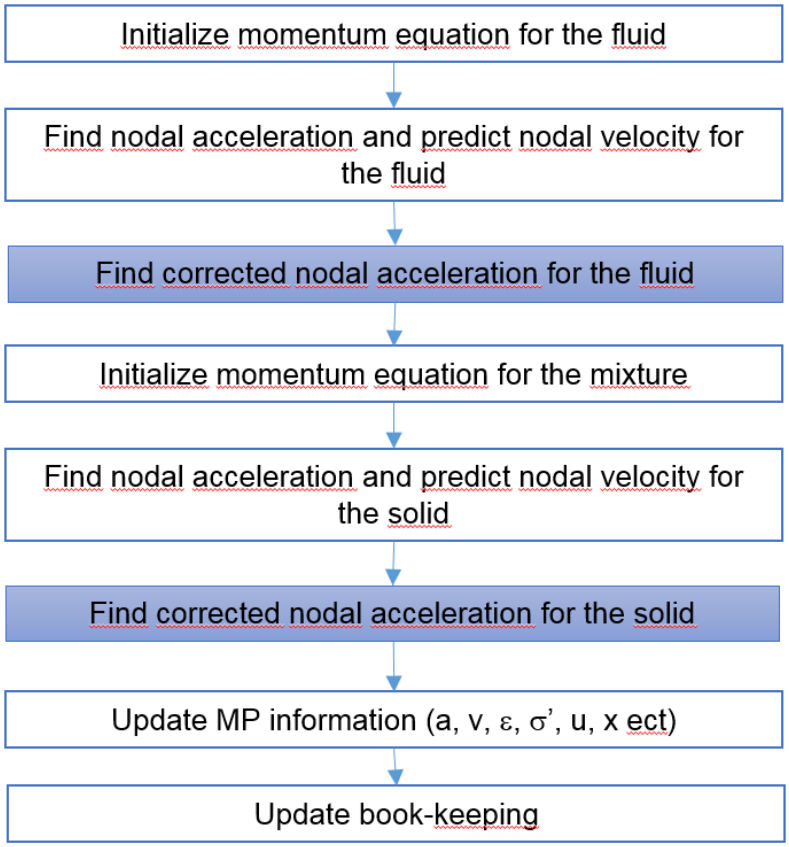

Figure 17 Computation scheme of two-phase MPM with contact algorithm.

PARAMETER	SYMBOL	VALUE
Virgin compression index [-]	λ	0.205
Recompression index [-]	κ	0.04
Effective Poisson's ratio [-]	ν'	0.25
Slope of CSL on p-q plane [-]	M	0.92
Initial void ratio [-]	e_0	1.41
Saturated density [kg/m^3]	ρ_{sat}	1700

Table 1 Material parameters used for the MCC model.

μ	q_d/q_{ref}	V_{50}	c
0.0	1.46	3.36	1.51
0.1	1.51	5.13	0.92
0.2	1.77	7.26	0.82
0.3	2.03	7.13	0.95
0.4	2.42	5.73	1.16

Table 2 Best fit of the coefficients in Equation 20 for different value of the friction coefficient μ.

Test site	depth	v'_{50} [mm/s]	c_v [m^2/s]	c_v [m^2/s]

			(this study)	(laboratory)
1	7.4-8.4	0.34	4.66E-06	5.82E-06
1	9.2-10.2	0.03	4.06E-07	4.67E-07
2	13-14	0.013	1.7E-07	3.64E-07

Table 3 Comparison between the coefficients of consolidation estimated with the proposed method and measured in the laboratory as reported by Kim et al. (2008)